

pubs.acs.org/JACS Article

# Degradation of FeNC Electrocatalysts for Acidic and Alkaline Oxygen Reduction

Weiwei Chen,<sup>#</sup> Yanyang Qin,<sup>#</sup> Changqi Heng, Shifu Wang, Mengshu Ge, Yangfan Li, Xin Wan, Xuning Li, Jianglan Shui,<sup>\*</sup> Yaqiong Su,<sup>\*</sup> and Dong Su<sup>\*</sup>



Cite This: J. Am. Chem. Soc. 2025, 147, 35730-35741



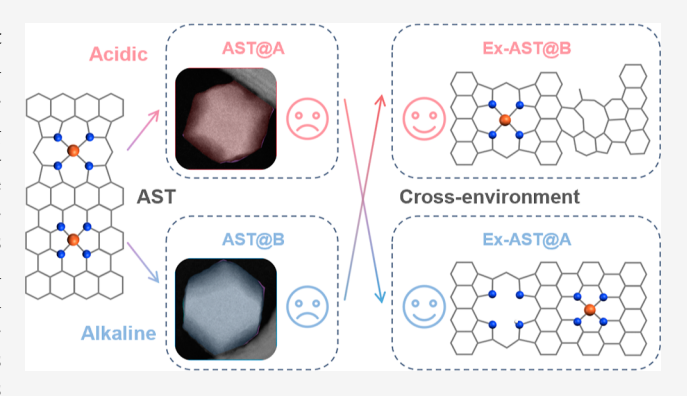
**ACCESS** I

III Metrics & More

Article Recommendations

s Supporting Information

ABSTRACT: Iron—nitrogen-carbon (FeNC) catalysts represent promising alternatives to platinum-group metals for the oxygen reduction reaction (ORR) in energy conversion technologies. However, their operational stability remains a critical challenge. In this study, we unravel the distinct degradation mechanisms and active-site behaviors of FeNC catalysts under acidic and alkaline ORR conditions. Intriguingly, catalysts subjected to electrochemical cycling in acidic media but tested in alkaline conditions exhibit nearly preserved ORR activity, revealing that degradation pathways differ fundamentally between the two environments. With the help of density functional theory calculations, we identify Fecentered sites as the primary active centers in acidic media, whereas under alkaline conditions—where hydroxyl adsorption passivates



Fe sites—neighboring carbon atoms adjacent to nitrogen become the dominant active sites. The Mössbauer spectroscopy results show that under acidic cycling, pyrrolic nitrogen-coordinated Fe (S1) sites suffer a significant loss while the pyridinic nitrogen-coordinated Fe (S2) sites retain high stability. In contrast, during alkaline cycling, Fe site losses are minimal, while the carbon support undergoes more severe corrosion. By selectively engineering the Fe sites and carbon support, we experimentally validated the conclusions on the active sites. This work provides critical insights into the site-dependent durability of FeNC catalysts and underscores the necessity of tailored catalyst design for stable and efficient ORR across diverse operating conditions.

#### ■ INTRODUCTION

Fuel cells, which electrochemically convert hydrogen or other fuels into electricity, hold great promise for a wide range of clean energy applications due to their high efficiency and low emissions. However, their widespread adoption depends on the development of cathodic oxygen reduction reaction (ORR) catalysts in terms of activity, stability and cost. Recently, single-atom catalysts have emerged as a breakthrough solution, offering maximized active sites, nearly 100% atomic utilization, and superior catalytic activity. Especially, iron—nitrogencarbon (FeNC) catalysts, exhibit the highest theoretical ORR activity, comparable to that of the benchmark Pt/C catalyst in numerous studies. Despite that, FeNC electrocatalysts also face significant challenges, particularly the performance degradation during prolonged cycling.

The demetalation of Fe and carbon oxidation reactions (COR) are recognized as the primary causes of degradation in FeNC electrocatalysts under acidic conditions.<sup>8</sup> FeN<sub>x</sub> sites are thermodynamically unstable at low pH, leading to the demetalation of Fe from the carbon support.<sup>9–11</sup> Additionally, protons may compete for the N<sub>x</sub> sites, further promoting the detachment of Fe.<sup>12,13</sup> The leached Fe cations can catalyze harmful reactions, generating reactive oxygen species (ROS)

that induce polarization and degrade performance. <sup>14</sup> In high-potential operational scenarios (>1.0 V), COR can lead to the loss of active sites, causing shrinkage or collapse, reduction in porosity, and loss of conductivity in the carbon support. <sup>15,16</sup> Even during cycling, ROS generated from incomplete ORR and Fenton reactions can trigger COR. <sup>17</sup> In such cases, COR can reduce the turnover frequency of FeN<sub>x</sub> sites and alter the wettability of the carbon surface, leading to micropore flooding. <sup>18,19</sup>

In alkaline conditions, FeNC electrocatalysts usually demonstrate enhanced stability due to the absence of protons. Similar degradation mechanisms to those observed under acidic conditions are believed to occur, though the influencing factors and extent may differ. However, recent studies suggest that the alkaline ORR may involve distinct active sites, such as carbon atoms adjacent to FeN<sub>4</sub>

Received: July 14, 2025 Revised: August 26, 2025 Accepted: September 5, 2025 Published: September 16, 2025





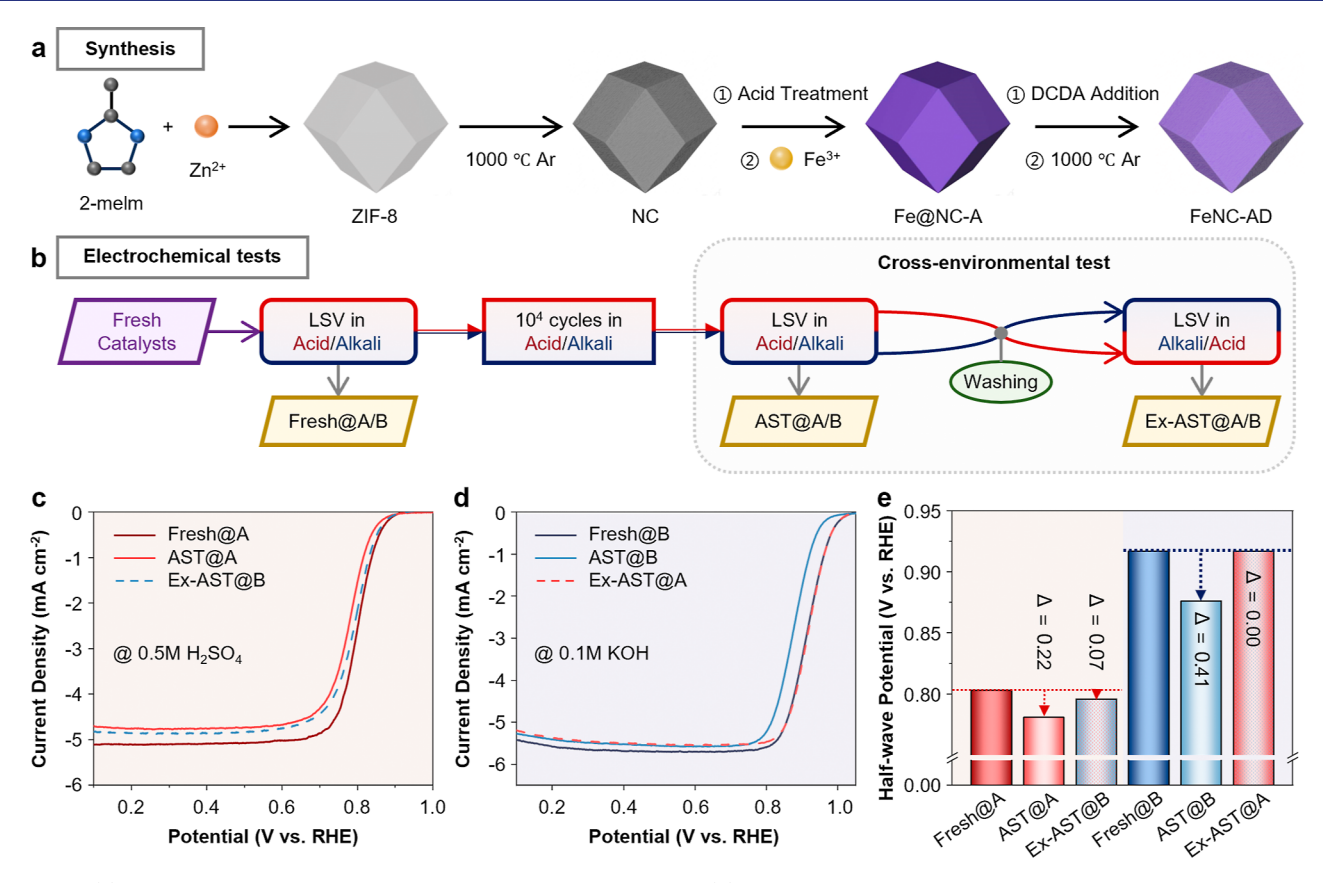


Figure 1. (a) Schematic illustration of the synthetic process for FeNC-AD. (b) Schematic representation of the RDE electrochemical protocols employed in this study. (c,d) ORR polarization curves of FeNC-AD measured under three different states (Fresh, AST, and Ex-AST) in (c) 0.5 M H<sub>2</sub>SO<sub>4</sub> and (d) 0.1 M KOH. (e) Comparison of the half-wave potentials of FeNC-AD under various conditions.

moieties.<sup>23</sup> These active sites are supposed to exhibit different degradation behaviors in alkaline media. Comparing the deactivation pathways in acid and alkaline media can be of great importance for designing highly stable electrocatalysts for ORR.

Given that a less pronounced structure-sensitivity of the ORR in alkaline electrolytes compared to acidic ones, 24 quantitatively elucidating the structural evolution of FeNC in alkaline media is challenging. Here, we utilize multiple quasi-in situ transmission electron microscopy (TEM) techniques, including energy-dispersive X-ray spectroscopy (EDS), and electron energy loss spectroscopy (EELS), as well as ex situ Mössbauer spectroscopy (MBS) to study the structural evolution in both acid and alkaline media. Notably, we introduce a cross-environmental test (CET), where, after conducting conventional accelerated stress test (AST) in one type of electrolyte, we test the electrocatalysts in another type of electrolyte. The purpose of CET is to assess varied degradation behaviors and the performance expression of electrocatalysts after ASTs under different environments. Further, by comparing the structural changes after different types of tests, we can correlate specific degradation mechanisms with acidic or alkaline active sites.

In this work, we elucidated the similarities and differences in degradation mechanisms that occur under acidic and alkaline conditions. Density functional theory (DFT) calculations confirmed that, under acidic conditions, pyrrolic nitrogencoordinated Fe (S1) sites have higher activity than pyridinic nitrogen-coordinated Fe (S2) sites. With a quantitative study on the structural evolution with comprehensive techniques, we

found that the acidic degradation primarily results from the leaching of S1 sites, whereas the alkaline instability is driven by carbon support corrosion and the loss of S2 sites. The distinct degradation mechanisms observed in acidic and alkaline environments underscored the complex interplay between electrocatalyst structure and environmental pH, revealing how different sites are selectively destabilized under varying conditions. This study provides novel insights into the stability of electrocatalyst and the degradation pathways in specific pH environments.

# RESULTS AND DISCUSSION

Synthesis and Electrochemical Performance of FeNC Electrocatalysts for Oxygen Reduction. We synthesized the FeNC electrocatalysts via a support precursor strategy,<sup>25</sup> which involved a two-step pyrolysis process of the ZIF-8 precursor, <sup>26</sup> as illustrated in Figure 1a. After the first pyrolysis at 1000 °C, an acid treatment was applied before metal impregnation. Dicyandiamide (DCDA) was then introduced during a second pyrolysis step at 1000 °C, yielding the final electrocatalyst (denoted as FeNC-AD). TEM images of Figure S1 show the morphologies of the FeNC-AD electrocatalysts, and X-ray diffraction analysis confirmed the absence of any metallic phases. The mass loading of Fe was determined to be 0.66 wt % using inductively coupled plasma optical emission spectroscopy. Aberration-corrected scanning transmission electron microscopy-high angle annular dark-field (STEM-HAADF) imaging study, complemented by EELS, confirms that Fe is isolated and atomically dispersed within the NC support (Figure S2).

We conducted electrochemical assessments using a rotating ring-disk electrode (RRDE) setup under oxygen-saturated conditions at room temperature. The electrochemical tests consisted of two main processes (Figure 1b): an AST and a CET (Figure S3). The AST involved 10,000 cyclic voltammetry (CV) cycles, where the voltage was varied between 0.60 and 0.95 V (vs RHE) at a scan rate of 50 mV/s. The resulting linear sweep voltammetry (LSV) curves were grouped into three distinct categories: untreated samples (Fresh@A/B), samples subjected to the AST (AST@A/B), and samples that underwent both AST and CET processes (Ex-AST@A/B). In this categorization, A and B refer to the two different initial test environments: A represents an acidic electrolyte of 0.5 M  $\rm H_2SO_4$ , while B corresponds to an alkaline electrolyte of 0.1 M KOH.

As shown in the electrochemical tests of Figure 1c,d, FeNC-AD exhibits superior performance in alkaline environments, with a half-wave potential  $(E_{1/2})$  of 0.92 V in comparison to 0.80 V in acidic media (Table S1). The hydrogen peroxide yields of FeNC-AD in both acidic and alkaline environments are below 1%, suggesting a four-electron (4e<sup>-</sup>) ORR pathway (Figure S4). Following ASTs, both the acidic- and alkalinetreated electrocatalysts exhibited significant performance degradation. The  $E_{1/2}$  values of AST@A and AST@B decreased by 22 mV and 41 mV, respectively, relative to their pristine state (Figure 1e). Additionally, changes in kinetic current density  $(j_k)$  mirrored the  $E_{1/2}$  trends (Figure S5 and Table S2). These findings suggest that degradation of FeNC-AD following ASTs is more pronounced in alkaline environment, challenging the conventional view of Fe single-atom catalysts degrading more in acidic conditions.<sup>9,22</sup>

To isolate the effects of the electrolyte and enable a comparable analysis of performance degradation in different environments, the CET was conducted. Specifically, the electrocatalysts after AST were cleaned and then retested in the other environment, i.e., the Ex-AST@A electrocatalysts underwent 10,000 potential cycles in acidic condition but were tested in alkaline media, and vice versa. The polarization curves (dashed lines in Figure 1c,d) reveal notable trends: Ex-AST@A exhibited near-fresh alkaline performance, with a  $\Delta E_{1/2}$  of approximately 0 mV, surpassing the AST@B. Additionally, Ex-AST@B, although still inferior to Fresh@A electrocatalysts, outperformed AST@A (Figure 1e). The  $j_k$  values also follow a consistent performance hierarchy: Fresh ≥ Ex-AST > AST across both acidic and alkaline environments (Figure S5). The retention of Ex-AST catalytic activity in the opposite electrolyte—despite prior degradation—suggests a reversible or environment-adaptive nature of certain structural degradation.

To determine whether this phenomenon represents a recovery of catalytic activity, the electrocatalysts were subjected to repeated transfers between environments after cleaning. E.g., Ex-AST@A was returned to acidic conditions. As shown in Figure S6, performance postreintroduction closely matched pre-exchange values, confirming that retained activity stemmed from intrinsic structural characteristics rather than transient postexchange recovery.<sup>27</sup> This result indicates that structural degradation induced by one electrolyte makes subdued contributions to the activity in another environment.

Morphological and Elemental Evolution of FeNC Electrocatalysts. To elucidate the structure—performance relationship of the electrocatalysts, it is critical to characterize their structural degradation after acidic and alkaline cycling. To

achieve this, we employed quasi-in situ TEM combined with EDS and EELS to track compositional and structural changes (Figure S7). The electrocatalysts were deposited on gold finder grids, enabling spatial tracking of predefined nanoregions across multiple degradation. Following the AST, we recharacterized the catalysts at identical locations (IL) using the same analytical techniques, minimizing sampling bias between pristine and degraded states.<sup>28</sup>

Figure S8 delineates the structural evolution of the electrocatalyst after cycling, revealing that both acidic and alkaline conditions induced structural alterations. Despite preserving the electrocatalyst's overall morphological integrity, its two-dimensional projection exhibited nuanced yet quantifiable compositional and structural variations. Differential mapping facilitated the spatial resolution of these variations, with purple-shaded areas indicating regions of contraction, and red/blue colorations representing zones of growth after AST under acidic and alkaline conditions, respectively. Notably, corrosion-induced contraction zones were predominantly found at the projections' corners, while redeposition-driven expansion zones were more commonly observed at the particle's periphery. We infer that during degradation, carbonaceous fragments that detach from the carbon support are likely redeposited via electrostatic adsorption rather than being fully released into the electrolyte. This observation suggests that the carbon support undergoes a structural evolution similar to particle degradation, driven by surfaceenergy minimization.<sup>29</sup> Figure S9 details the application of lowloss EELS to quantify thickness variations.<sup>30</sup> We found that mass conservation was preserved at the macroscale under both acidic and alkaline conditions. Line-scanning measurements further confirmed that thickness values remained nearly identical before and after AST. These results indicate that the electrocatalyst's three-dimensional morphology exhibits consistent structural stability across the macroscopic surface.

In addition to monitoring structural changes, we tracked compositional evolution before and after potential cycling with IL-STEM-EDS. Figures S10 and S11 present the EDS mappings at various degradation stages, depicting the spatial distribution of C, N, O, and Fe within the electrocatalyst particles. To ensure accurate compositional analysis, we selectively integrated EDS signals within the defined particle contour regions, thereby excluding nontarget contributions (Figure S12). The collected data were systematically summarized in Tables S3 and S4, respectively. As revealed by the percentage stacking chart (Figure S13), we observed a significant decrease in carbon content accompanied by proportional increases in nitrogen and oxygen signals. The increase of oxygen may stem from support oxidation and adsorbed oxygen intermediates. In contrast, no external nitrogen sources contributed to the postreaction nitrogen composition, underscoring its quantitative stability within the electrocatalyst framework under all tested conditions. Detailed N-K edge EELS analysis (Figure S14) provided insights into the nitrogen coordination environments. The N-K edge spectrum remained essentially unchanged after acidic AST, with only a minor emergence of a 399.7 eV peak, which corresponds to nitrilic forms,<sup>31</sup> suggesting that some nitrogen atoms were protonated. Following the alkaline AST, a prominent peak appeared at 401.2 eV. Control experiments showed this feature appeared in alkaline ex situ measurements but was absent in simple soaking tests (Figure S15). While multiple factors could potentially explain this spectral

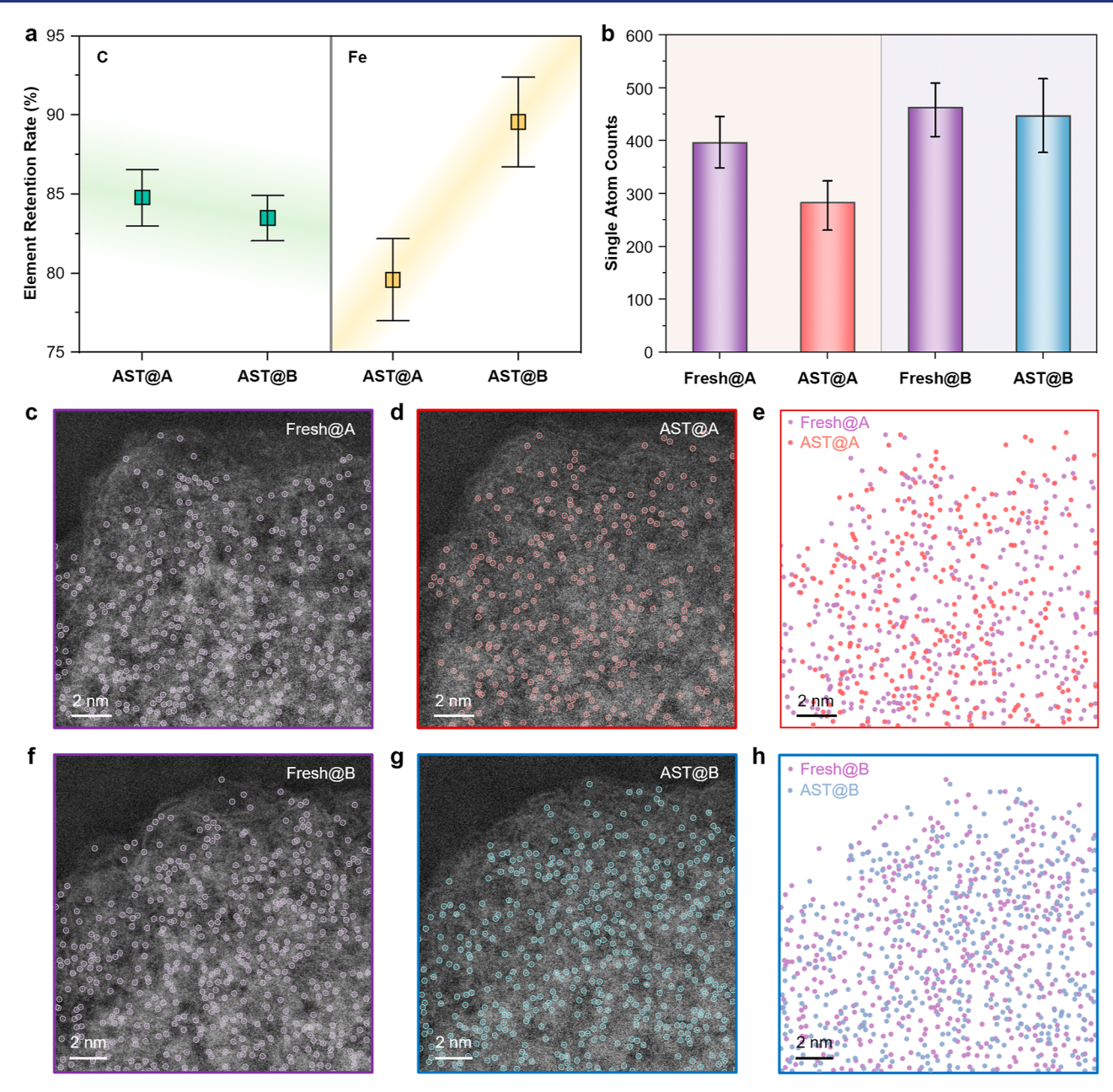


Figure 2. (a) Quantitative comparison of the carbon and iron retention rates after acidic and alkaline AST. (b) Number of detected single atoms from STEM-HAADF images, with error bars obtained by a  $\pm 5\%$  detection threshold. (c-h) Quasi-in situ STEM-HAADF images and corresponding graphical representations of identified atoms, showing overlap at identical locations under acidic (c-e) and alkaline (f-h) conditions.

change,<sup>32</sup> its complete disappearance after the CET strongly suggests that it arises from modulation of nitrogen electronic states by nearby adsorbates (e.g., hydroxide ions adsorbed on adjacent carbon sites) rather than permanent nitrogen modification.<sup>33</sup> These observations provide evidence for the stability of nitrogen species throughout the electrochemical cycling in both acidic and alkaline environments.

To further quantify compositional changes, we extracted IL-EDS signals of carbon and iron from electrocatalysts undergoing different ASTs (Figure 2a). For quantitative analysis, these signals are normalized with respect to the nitrogen EDS signal. The retention of the carbon signal showed a slight discrepancy, with approximately 85% retention under acidic condition compared to roughly 83% under alkaline condition. This result suggests that the C element was

lost in both acid and alkaline conditions, likely due to carbon oxidation and subsequent conversion into  $CO_2$ , which then escaped. The discrepancy suggests that the stability of the carbon support is relatively lower during alkaline cycling. In contrast, Fe demonstrated a pronounced degradation pattern: a loss of approximately 20% in acidic conditions, about twice the loss observed in alkaline media (10%). This result agrees with metal's known vulnerability to acidic corrosive conditions, where demetalation dominates. The EDS signals of C and Fe after the CET exhibited minimal changes (<5%, Figure S16) comparing to the signals before exchanging (Figure 2a), which suggests that the CET would not affect the chemical compositions of electrocatalysts.

**Evolution of Iron Species in FeNC Electrocatalysts.** To elucidate the stability of Fe single-atom sites under electro-

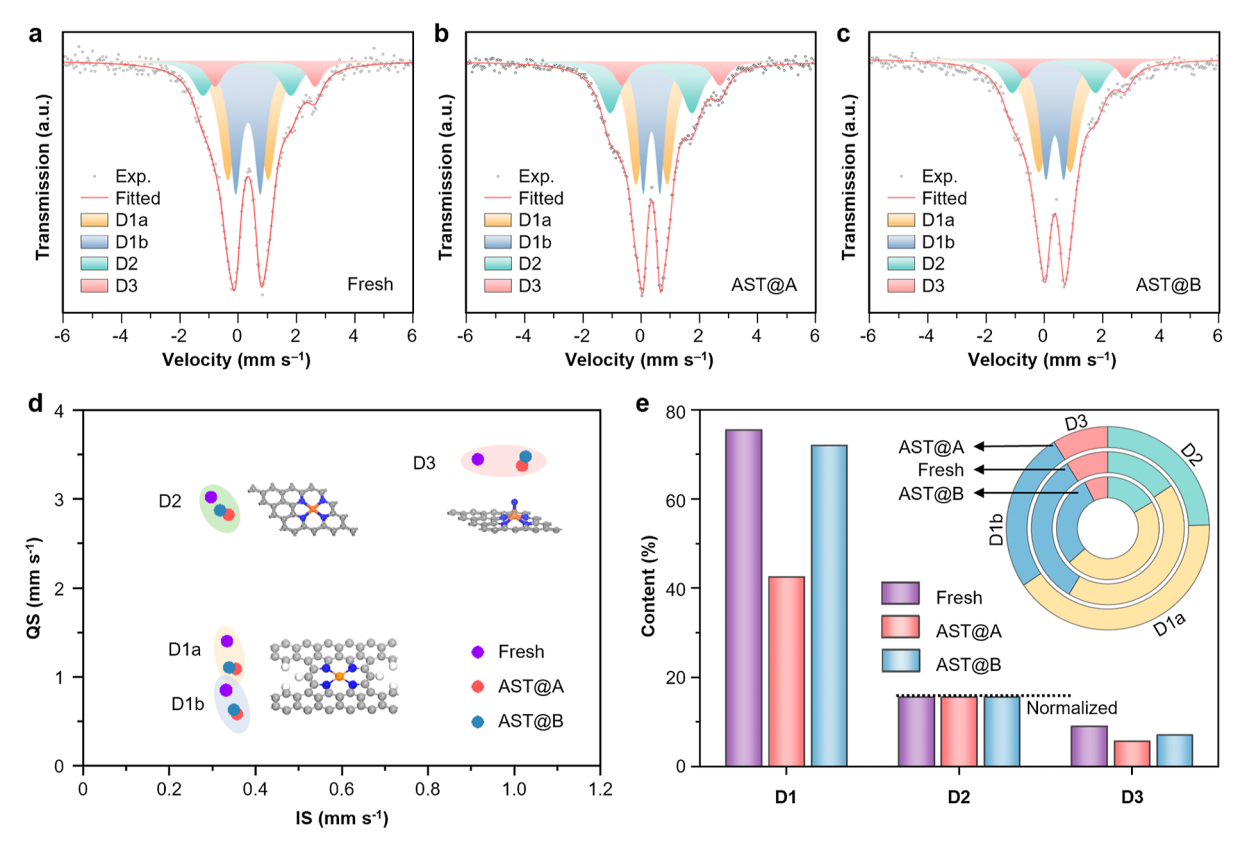


Figure 3. (a–c) The <sup>57</sup>Fe Mössbauer spectra of FeNC-AD: (a) fresh, (b) after acidic AST, and (c) after alkaline AST. Exp., experimental. (d) Isomer shift (IS) and quadrupole splitting (QS) values for components D1, D2, and D3, with their corresponding structures. (e) Relative content of different Fe moieties under varying conditions, normalized to D2. Inset: a fan chart illustrating the distribution of Fe moieties.

chemical conditions, we performed atomic-resolution STEM-HAADF imaging before and after ASTs (Figure 2b-h). Remarkably, IL-STEM-HAADF characterization demonstrated the preservation of well-dispersed single-atom Fe species under both acidic (Figure 2c,d) and alkaline (Figure 2f,g) conditions after ASTs. For precise atomic-scale analysis, we implemented a machine learning (ML)-based algorithm with standardized parameters and detection thresholds to accurately localize Fe sites.<sup>36</sup> Comparative spatial distribution analyses before and after ASTs (Figure 2e,h), corroborated by nearest-neighbor distance statistics (Figure S17), confirmed the absence of aggregation tendencies. Complementary characterization of AST@A/B samples further excluded any Fe nanoparticle formation (Figure S18), thereby eliminating agglomeration or phase transformation as potential degradation mechanisms. Quantitative analysis revealed striking environmental dependence: acidic cycling induces substantial Fe depletion (~30%), while alkaline cycling causes minimal Fe loss (<5%) (Figure 2b). The consistency between these quantitative results and EDS measurements, when combined with direct atomicresolution imaging evidence, provides confirmation that Fe loss occurs through individual atom detachment rather than through any collective processes.

After the CET, the distribution of Fe single atoms was visualized in STEM-HAADF images (Figure S19). Upon introducing AST@A to alkaline conditions, the number of Fe atoms in the same region remained nearly constant. However, when AST@B was introduced to acidic conditions, a further loss of Fe was observed, resulting in a final Fe retention of approximately 87%. These results suggest that a subpopulation of single-atom Fe sites remains stable under alkaline conditions

but is unstable under acidic conditions. After the removal of these Fe atoms in AST@B, the proportion of residual Fe atoms still significantly exceeded the Fe content observed in AST@A, further confirming the enhanced stability of Fe during alkaline AST.

To gain further insights into the correlation between the stability and the Fe coordination environment, we employed ex situ <sup>57</sup>Fe MBS, which enabled the identification of distinct Fe species in the single-atom state. The degraded electrocatalysts were extracted from the membrane electrode assemblies after electrochemical testing (Figure S20). These electrocatalysts exhibited the same overarching degradation trends as observed in RDE experiments across all tested conditions.<sup>37</sup>

The three Mössbauer spectra for Fresh, AST@A, and AST@ B electrocatalysts were primarily fitted with four doublets attributed to distinct coordination geometries (Figure 3a-c). Their isomer shifts (IS) and quadrupole splitting (QS) values and structural assignments for each species are summarized in Figure 3d. The D1 doublet consists of D1a and D1b, which are assigned to high-spin (HS) Fe<sup>3+</sup> and low-spin (LS) Fe<sup>2+</sup>, respectively. 38,39 It shows low IS and QS values, suggesting an association of Fe with pyrrolic nitrogen-donor moieties (S1). The doublet D2 was attributed to low or intermediate-spin (MS) Fe<sup>2+</sup>, with the Fe nucleus coordinating to four pyridinic nitrogen ligands (S2).<sup>4,38</sup> Doublet D3 corresponds to HS Fe<sup>2+</sup>, exhibiting a significantly larger IS than D1 and D2. This suggests that the Fe atom is displaced from the N<sub>4</sub> plane, likely due to an additional interaction with one of the existing nitrogen atoms, effectively creating a fifth coordination site.<sup>4</sup>

After the electrochemical cycling, the nuclear environments of various species were altered. The diminished QS in D1 and

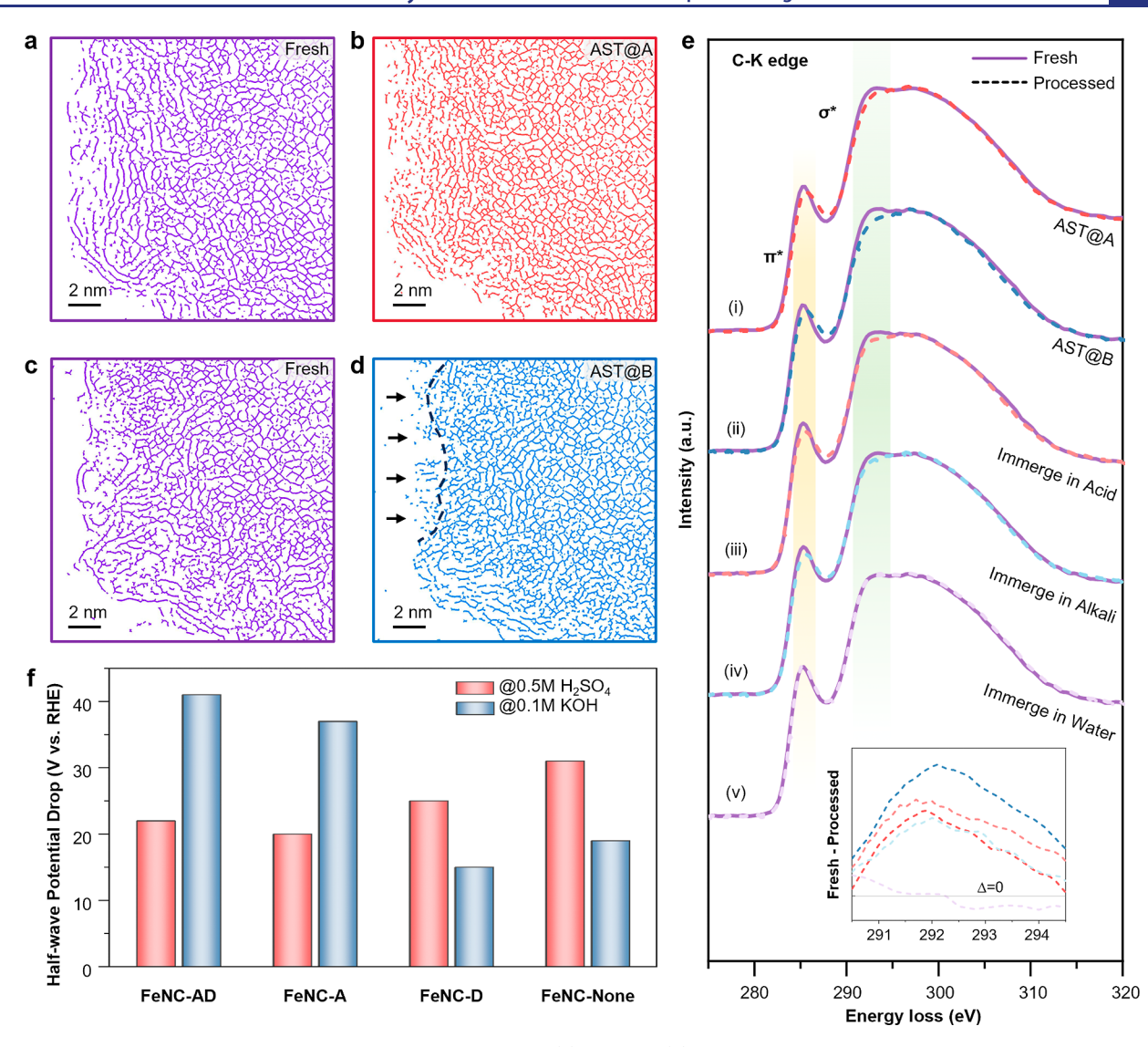


Figure 4. Skeletonized STEM-BF images of carbon framework before (a) and after (b) 10,000 cycles of AST under acidic condition, ibid before (c) and after (d) 10,000 cycles of AST under alkaline condition. The arrows indicate the region of severe degradation outside the dashed line. (e) C–K edge EELS spectra for FeNC-AD under various conditions: before and after (i) acidic AST, (ii) alkaline AST, (iii) immersion in acidic media, (iv) immersion in alkaline media, and (v) immersion in deionized water. Inset: The difference in spectral intensity before and after processing. (f) Comparison of the half-wave potential drop for FeNC-AD, FeNC-D, and FeNC-None after ASTs in acidic and alkaline electrolytes.

D2 was attributed to the adsorption of reaction intermediates (e.g., hydroxyl groups) on the Fe centers. 40 The elevated IS observed in D3 suggests a modified coordination environment of Fe atoms, presumably due to interaction with Nafion sulfonic groups. 41 Quantitative data from Table S4 detail the relative abundance of Fe species across conditions. The conversion of S1 to S2 sites is hindered by a large energy barrier. 42 For clarity in visualization, D2 values were normalized to emphasize relative changes (Figure 3e). In acidic conditions, the combined loss of D1 and D3 (10:1) fully accounts for the total Fe decline observed in TEM, implying that S2 sites remain stable. In alkaline conditions, however, the experimental Fe loss (~10% by EDS) exceeds the predicted loss (~5%) if S2 sites stability were assumed, implying degradation of S2 sites also occurs under alkaline cycling. Additionally, the increase in the D1a/D1b ratio suggests that S1 FeN<sub>4</sub> sites undergo oxidation during potential cycling (Figure 3e inset). 12

The observed catalytic activity decline in acidic environments can be attributable to the loss of S1 Fe sites—principle

contributors to active site density (discussed later). <sup>41</sup> Conversely, under alkaline conditions, significant degradation persists despite negligible changes in the quantities of Fe species. This disparity indicates that factors beyond atomic Fe depletion play a dominant role in alkaline-mediated performance loss.

Carbon Corrosion in FeNC Electrocatalysts. Although EDS results indicate similar carbon loss rates under acidic and alkaline conditions (Figure 2a), the actual degradation of the FeNC carbon support may vary between pH environments, particularly in terms of corrosion patterns, lattice fragmentation, and graphitic order. To resolve these structural differences, we first employed STEM-BF imaging to directly visualize the morphological evolution of the carbon support under acidic versus alkaline cycling conditions (Figure S21). For enhanced detection of fine-scale structural changes, we utilized a ML-based edge detection method that integrated Gaussian mixture model (GMM)-driven thresholding with morphological skeleton extraction algorithms. The resulting

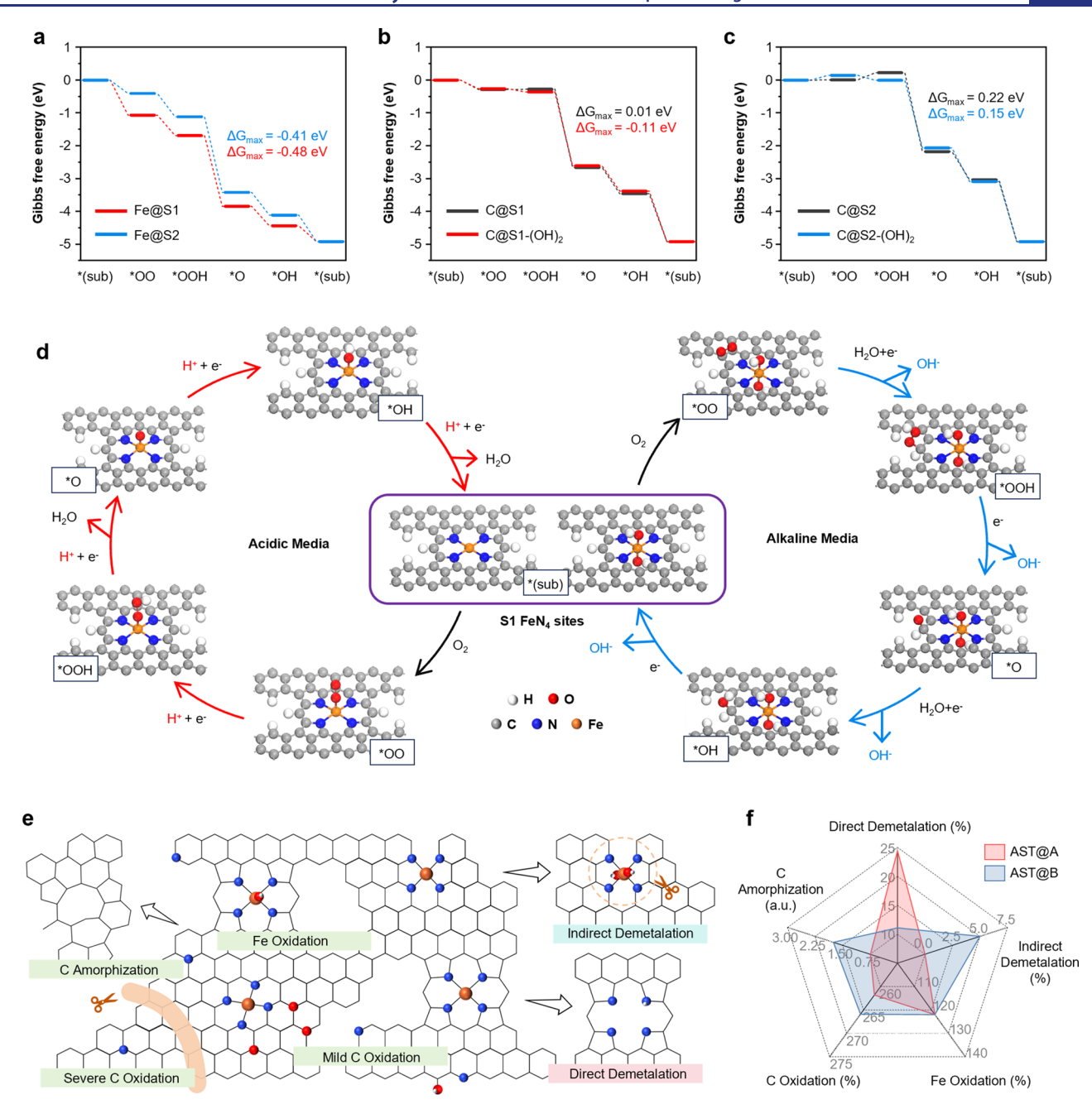


Figure 5. (a) Free energy diagram elucidating the 4e<sup>-</sup> associative pathway of the ORR on S1 and S2 sites with Fe as the active site. (b) Free energy diagram comparing the ORR on S1 sites with and without hydroxyl ligands, using C as the active site. (c) Free energy diagram comparing the ORR on S2 sites with and without hydroxyl ligands, using C as the active site. (d) Schematic representation of the ORR pathway on S1 FeN<sub>4</sub> electrocatalysts, illustrating the reaction mechanisms at Fe and C active sites under acidic and alkaline conditions, respectively. (e) Schematic illustration of the degradation mechanisms of FeNC electrocatalysts. (f) Comparison of acidic and alkaline degradation mechanisms.

visualizations are presented in Figure 4a—d. The electrochemical cycling in both acidic and alkaline led to detrimental fragmentation of the continuous graphene-like pathways, converting them into disconnected nanometric domains, especially at the edge of the support. Notably, alkaline conditions induced more severe corrosion, with the initial lattice continuity being extensively fragmented (arrow-marked regions in Figure 4d), exceeding the corrosion observed under acidic conditions (Figure 4b).

We then performed EELS analysis of the C-K edge to characterize the electronic structure and bonding states of the carbon support (Figure 4e). All spectra were normalized with

respect to the C–K edge shoulder region (40 eV post to the threshold position). The pristine carbon signal exhibited two principal peaks: a low-energy peak at approximately 285 eV (1s  $\rightarrow \pi^*$ , P1) and a high-energy contribution starting around 292 eV (1s  $\rightarrow \sigma^*$ , P2). The postcycling spectra from both (i) acidic and (ii) alkaline conditions displayed decreases of P1, which suggests reduced graphitization. The accurate quantification of the P1 intensity reduction was complicated by the overlapping contribution of the CO bond signal at ~286 eV. A distinct difference emerged between 291 and 294 eV, corresponding to long-range sp² hybridization order,<sup>31</sup> with AST@B showing more pronounced attenuation (Figure 4e inset).

To decouple chemical and electrochemical contributions to carbon corrosion, we performed quasi-in situ experiments by immersing fresh electrocatalysts in three environments for 40 h: (iii) 0.5 M H<sub>2</sub>SO<sub>4</sub>, (iv) 0.1 M KOH, and (v) deionized water (Figure 4e). EELS analysis revealed negligible changes in the carbon support after water immersion, confirming that neither passive hydration nor the measurement process induced structural degradation. In contrast, both acidic and alkaline immersion led to a reduction in C-K edge intensity. The attenuation around 293 eV was comparable to that observed after acidic AST (AST@A) but less pronounced than after alkaline cycling (AST@B). This indicates that the degradation of support during acidic AST is primarily due to chemical reactions, whereas under alkaline potential cycling, the degradation process is influenced by a synergistic combination of electrochemical corrosion and chemical processes. A prior study indicated that mere electrolyte immersion does not alter catalytic performance.44 Thus, the performance decline observed after alkaline AST likely arises from electrochemical corrosion mechanisms that uniquely destabilize the carbon support under potential cycling.

Influence of Fe Species and Carbon Support on Electrochemical Performance and Stability. Our above studies identified distinct degradation pathways for FeNC-AD electrocatalysts under acidic and alkaline conditions during long-term cycling: acidic environments predominantly promote Fe leaching, whereas alkaline media induce electrochemical corrosion of the carbon support. These observations suggest that different active sites may govern performance in each electrolyte—Fe-centered sites dominating in acid and carbon-based sites in alkaline media. To systematically investigate how Fe species and carbon support properties influence these pH-dependent behaviors, we designed controlled catalyst modifications for comparative stability analysis.

The FeNC-AD electrocatalyst was synthesized undergoing two key steps: subjecting the NC precursor to acid treatment and incorporating DCDA during the second pyrolysis step. Prior research has shown that while acid pretreatment facilitates Fe metalation, 26 it simultaneously generates structural defects through C-C bond cleavage. 45 DCDA functions as an additional nitrogen source and modulates Fe speciation. 46,47 Based on these findings, we designed three controlled electrocatalyst variants: (1) FeNC-A, prepared with acid etching but without additional nitrogen doping; (2) FeNC-D, synthesized with DCDA doping but without acid pretreatment; and (3) FeNC-None, an unmodified reference catalyst subjected to neither treatment (Figure S22). Comparing these samples with FeNC-AD electrocatalyst is to decouple the individual contributions of Fe-related species and carbon support properties to the overall electrocatalytic performance.

Following the same experimental protocol detailed in Figure 1b, we conducted electrochemical tests of three additional electrocatalysts, as shown in Figure S23. All tested electrocatalysts exhibited consistent performance trends across three key stages (Fresh, AST, and EX-AST), maintaining the identical activity hierarchy (Fresh  $\geq$  EX-AST > AST) originally established for the FeNC-AD electrocatalysts. The FeNC-D and FeNC-AD electrocatalysts exhibited enhanced initial activity in acidic media while maintaining comparable alkaline performance to DCDA-undoped samples (Figure S24), indicating that Fe speciation modifications specifically

influence acidic properties without affecting alkaline behavior. In contrast, acid-pretreated NC supports may improve the activity of FeNC electrocatalysts in both acidic and alkaline electrolytes (FeNC-AD vs FeNC-D and FeNC-A vs FeNC-None; Figure S24), presumably through increased surface area and consequent proliferation of accessible active sites. <sup>48</sup>

To evaluate their stability, we monitored the  $E_{1/2}$  shift after 10,000 cycles of these electrocatalysts in different electrolytes (Figure 4f). While DCDA modification showed negligible effects on stability ( $\Delta E_{1/2}$  changes lacked consistent trends), acid pretreatment of the NC precursor profoundly influenced degradation behavior. Acid-treated electrocatalysts (FeNC-AD and FeNC-A) exhibited high stability in acidic media ( $\Delta E_{1/2} \approx$ 20 mV) but significant alkaline degradation ( $\Delta E_{1/2} \approx 40$  mV). Conversely, nonacid-treated electrocatalysts (FeNC-D and FeNC-None) demonstrated poor acid stability ( $\Delta E_{1/2} > 25$ mV) yet enhanced alkaline resilience ( $\Delta E_{1/2}$  < 20 mV). Control experiments with Fe-free supports (NC-A and NC-None, Figure S25) further revealed that NC-A suffered severe alkaline instability, whereas NC-None maintained exceptional stability. These results unequivocally demonstrate that modifications to carbon support directly govern alkaline stability, while Fe speciation primarily dictates acidic perform-

Theoretical Explanation. To gain a more comprehensive understanding, DFT calculations were conducted to evaluate the intrinsic catalytic activity of different sites within the FeNC electrocatalyst system (Figure 5). The maximum free energy changes ( $\Delta G_{\text{max}}$ ) along the 4-electron associative pathway for ORR over the S1 sites and S2 sites were calculated (Figure 5a). The  $\Delta G_{\text{max}}$  obtained over the S1 sites (-0.48 eV) is lower than that for the S2 sites (-0.41 eV). This result indicates that Fe coordinated with pyrrole nitrogen has higher catalytic activity, which is consistent with previous reports. 41,42 However, in alkaline environments, the role of metal sites can be inhibited, as many researchers have reported that alkaline performance remains largely unchanged after the addition of various anions, such as SCN-, F-, and Cl-, which can poison the metal centers at the active sites. 49 Given the hydroxide-rich nature of alkaline environments, we calculated the binding energies of the first and second hydroxide at the S1 and S2-type FeN<sub>4</sub> sites (Figure S26), which were found to be -2.80 eV and -2.61 eV for the first hydroxide, and -2.88 eV and -2.71 eV for the second hydroxide, respectively. The calculated binding energies demonstrate strong hydroxide affinity for both S1 and S2 sites, with all values exceeding -2.6 eV. These thermodynamically favorable interactions indicate that multiple hydroxyl ligands can spontaneously coordinate to the Fe centers under alkaline conditions, thereby hindering Fe as an active center and improving its stability during cycling.<sup>50</sup> Many researches have reported that the carbon atoms adjacent to the N sites can serve as active centers in nitrogen-doped carbon system. For instance, atoms adjacent to the nitrogen in pyridine serve as Lewis base sites promoting ORR,<sup>51</sup> while carbons located at Zigzag edges are also recognized as active centers.<sup>52</sup> To elucidate the role of neighboring carbon atoms in alkaline catalytic activity, we investigated their behavior both with and without axial adsorption of two hydroxyl groups on Fe sites. The free energy diagram illustrates that the edge carbon site in the S1-type structure exhibits catalytic activity, achieving a  $\Delta G_{\rm max}$  of -0.11 eV while two hydroxides adsorbed on the Fe atom (Figure 5b), which is lower than that in the bare FeN<sub>4</sub> system (0.01 eV). Similar trends are observed for the S2-type

system, with a  $\Delta G_{\rm max}$  of 0.15 eV for the system with two axial adsorptions versus 0.22 eV for the bare system (Figure 5c). These carbon sites may demonstrate improved catalytic performance in alkaline environments, indicating that FeN<sub>4</sub> system could exhibit distinct active centers in acidic and alkaline conditions (Figures 5d and S27).

Additionally, we calculated the binding energy of carbon to assess the stability of the support (Figure S28). The binding energy of carbon atoms in the graphene structure distant from nitrogen atoms is lower than that of carbon atoms adjacent to a nitrogen atom, suggesting that nitrogen doping may decrease the stability of carbon and compromise its corrosion resistance.<sup>34</sup> Furthermore, we also investigated the effect of hydroxyl adsorption over Fe sites on the stability of carbon atoms (Figure S28). The results show that, in the pyrrole nitrogen-coordinated system, hydroxyl adsorption has a relatively less effect on the binding energy of carbon, whereas, in the pyridine nitrogen-coordinated system, hydroxyl adsorption significantly increases the binding energy of carbon adjacent to the nitrogen atom by more than 1 eV (from -5.92 eV to -4.86 eV) thereby reducing the stability of the S2 sites.

Structure-Activity-Degradation Relationships in **FeNC Electrocatalysts.** Figure 5e summarizes the degradation mechanisms, and Table S6 presents the corresponding supporting evidence and inferences. Degradation pathways under acidic and alkaline conditions share common features but diverge in key mechanistic aspects. Nitrogen species exhibit remarkable stability in both quantity and speciation, with no evident pathways for their elimination. Carbon oxidation occurs in both environments, with mild oxidation being partially reversible—mediated by oxygen species adsorbed on the carbon surface. 18 In contrast, severe oxidation drives irreversible structural degradation through CO2 evolution, resulting in direct carbon loss. Furthermore, the carbon support progressively amorphizes. Hydroxyl species may adsorb onto iron sites, inducing slight Fe-oxidation, while concurrent demetalation further destabilizes the Fe centers.

The primary difference between acidic and alkaline conditions lies in the mechanisms and extent of degradation. Acidic conditions primarily drive the chemical degradation of the support, while alkaline environments accelerate deterioration through coupled electrochemical and chemical pathways. Acidic media induce direct demetalation via proton-assisted metal dissolution from nitrogen coordination sites. Although alkaline conditions also allow for direct demetalation, this effect is less pronounced due to reduced proton availability. However, alkaline conditions uniquely facilitate indirect metal loss due to the instability of S2 sites. To quantitatively compare these degradation pathways, we utilize several structural and compositional metrics (Figure 5f; detailed in the Supporting Information Notes) to assess the extent of degradation under acidic and alkaline conditions.

Next, we aim to establish the relationship between structure and performance. Although experimental performance metrics are indirectly related to the active sites, they can be interpreted as reaction rates, calculated as the sum of the products of the various types of active site densities and their intrinsic reactivities, provided that convoluting factors are adequately controlled.<sup>53</sup> Based on the performance data of the electrolyte exchange experiment and the characterization of the degraded electrocatalyst, we can obtain the following formula (detailed in the Supporting Information Notes)

acid activity = 
$$a_1 \cdot F_1 + a_2 \cdot F_2 + A$$
 (1)

alkaline activity = 
$$b_2 \cdot F_2 + b_3 \cdot C_N + B$$
 (2)

Here,  $F_1$  and  $F_2$  represent the density of S1 and S2 sites, respectively, and  $C_N$  represents the density of the active carbon mostly near nitrogen (not all carbon atoms). The weighting coefficients  $a_i$  (i=1,2) and  $b_j$  (j=2,3) are related to the nature of the activity of different species. A and B include all other error terms, such as synergistic effects between different sites, other potential active sites (which may be present in small quantities or exhibit low activity in our system), and so on. These terms are considered constant to some extent.

Formula 1 demonstrates that carbon-based sites contribute minimally to catalytic activity compared to Fe moieties in acidic media. Based on the results of DFT calculations, we propose that the coefficient  $a_1$  is greater than  $a_2$ . As shown in formula 2, while S1 sites exhibit significant intrinsic activity in acidic conditions, their contribution to ORR performance in alkaline conditions appears negligible. In contrast, alkaline activity is primarily mediated by S2 sites and nitrogencoordinated carbon sites. The persistent inclusion of the  $b_2$ · $F_2$  term in the alkaline activity model may result from the indirect demetalation pathway unique to S2 sites, which generates strong covariance between S2 site depletion and carbon corrosion.

The corresponding degradation can also be calculated by

$$\Delta \text{acid activity} = a_1 \cdot \Delta F_1 + \delta \tag{3}$$

$$\Delta \text{alkaline activity} = b_2 \cdot \Delta F_2 + b_3 \cdot \Delta C_N + \delta \tag{4}$$

Here,  $\delta$  represents a small term accounting for potential errors or other negligible factors. After electrochemical cycling in acidic and alkaline environments, the electrocatalysts' performance deteriorates due to the loss of their active components. Compared to fresh electrocatalysts, the S2 site of the AST@A electrocatalyst remains stable, and the support does not degrade by electrochemical effect, resulting in performance comparable to that of the initial electrocatalyst in alkaline environments. Furthermore, the content of S1 sites in the AST@B electrocatalyst is intermediate between that of the fresh and AST@A electrocatalysts, which correlates with their observed performance.

## CONCLUSION

This study offers a comprehensive analysis of the electrochemical performance and degradation mechanisms of FeNC electrocatalysts for the ORR in acidic and alkaline environments. STEM-BF imaging reveals extensive fragmentation of graphene-like domains, while EELS confirms the loss of longrange sp<sup>2</sup> hybridization order. With the help of DFT, we identify that in acidic environments, activity is dominated by Fe sites (S1 and S2), with minimal contributions from the carbon support. Under these conditions, Fe demetalationespecially from S1 sites—is identified as the dominant degradation pathway, as evidenced by atomic-resolution STEM-HAADF imaging and Mössbauer spectroscopy. In contrast, under alkaline AST, severe performance degradation arises from electrochemical corrosion of the carbon support. Therefore, FeNC electrocatalysts cycled in acidic media but tested in alkaline environments (Ex-AST@A) retain near-fresh performance, as acidic Fe demetalation does not impair alkaline-active sites. Conversely, FeNC electrocatalysts cycled in alkaline media but tested in acidic conditions (Ex-AST@B)

exhibit partial performance recovery, as carbon corrosion in alkaline environments has little influence on the acidic-active sites. Comparative studies on four controlled electrocatalysts elucidate the distinct roles of Fe species and carbon support properties in acidic and alkaline performance. Introducing DCDA, which modifies Fe speciation, significantly enhances acidic performance but has negligible impact on alkaline media. Furthermore, we found that acid pretreatment of the carbon support has a minimal impact on acidic durability but leads to severe degradation in alkaline ORR, supporting our conclusions on the active sites. Importantly, this work uncovers a previously unrecognized regenerative capability: FeNC catalysts that degraded in acidic media can deliver high performance in alkaline media. This unexpected resilience challenges the conventional paradigm of irreversible catalyst degradation and opens new avenues for the reuse and recycling of electrocatalysts across different operating environments. These findings deepen our understanding of FeNC catalyst degradation mechanisms and offer valuable guidance for the rational design of durable ORR catalysts for next-generation fuel cells.

#### ASSOCIATED CONTENT

# Supporting Information

The Supporting Information is available free of charge at https://pubs.acs.org/doi/10.1021/jacs.5c11985.

> Experimental details, additional characterization data, electrochemical and computational methodologies, and supplementary analyses of degradation mechanisms (PDF)

# AUTHOR INFORMATION

# **Corresponding Authors**

Jianglan Shui - School of Materials Science and Engineering, Beihang University, Beijing 100191, China; orcid.org/ 0000-0002-5935-5733; Email: shuijianglan@buaa.edu.cn

Yaqiong Su - School of Chemistry, Engineering Research Center of Energy Storage Materials and Devices of Ministry of Education, National Innovation Platform (Center) for Industry-Education Integration of Energy Storage Technology, Xi'an Jiaotong University, Xi'an 710049, China; orcid.org/0000-0001-5581-5352; Email: yqsu1989@ xitu.edu.cn

**Dong Su** – Beijing National Laboratory for Condensed Matter Physics, Institute of Physics, Chinese Academy of Sciences, Beijing 100190, China; University of Chinese Academy of Sciences, Beijing 100049, China; orcid.org/0000-0002-1921-6683; Email: dongsu@iphy.ac.cn

#### Authors

Weiwei Chen - Beijing National Laboratory for Condensed Matter Physics, Institute of Physics, Chinese Academy of Sciences, Beijing 100190, China; University of Chinese Academy of Sciences, Beijing 100049, China

Yanyang Qin - School of Chemistry, Engineering Research Center of Energy Storage Materials and Devices of Ministry of Education, National Innovation Platform (Center) for Industry-Education Integration of Energy Storage Technology, Xi'an Jiaotong University, Xi'an 710049, China

Changqi Heng – State Key Laboratory of Catalysis, Dalian Institute of Chemical Physics, Chinese Academy of Sciences, Dalian 116023, P. R. China

Shifu Wang - State Key Laboratory of Catalysis, Dalian Institute of Chemical Physics, Chinese Academy of Sciences, Dalian 116023, P. R. China

Mengshu Ge - Beijing National Laboratory for Condensed Matter Physics, Institute of Physics, Chinese Academy of Sciences, Beijing 100190, China

Yangfan Li - Beijing National Laboratory for Condensed Matter Physics, Institute of Physics, Chinese Academy of Sciences, Beijing 100190, China; University of Chinese Academy of Sciences, Beijing 100049, China

Xin Wan - School of Materials Science and Engineering, Beihang University, Beijing 100191, China; orcid.org/ 0000-0002-6435-1761

Xuning Li - State Key Laboratory of Catalysis, Dalian Institute of Chemical Physics, Chinese Academy of Sciences, Dalian 116023, P. R. China; orcid.org/0009-0009-7353-842X

Complete contact information is available at: https://pubs.acs.org/10.1021/jacs.5c11985

#### **Author Contributions**

\*W.C. and Y.Q. contributed equally.

The authors declare no competing financial interest.

## **ACKNOWLEDGMENTS**

This work was supported by the National Key Research and Development Program of China (2023YFB4006200), the National Natural Science Foundation of China (No. U21A20328 and 22209202) and the Strategic Priority Research Program of the Chinese Academy of Sciences (XDB0600200). The AI-driven experiments, simulations and model training were performed on the robotic AI-Scientist platform of Chinese Academy of Sciences. Y.S. acknowledged the funding by Key Research and Development Program of Shaanxi Province (2025SF-YBXM-526) and Shaanxi Fundamental Science Research Project for Chemistry and Biology (Grant No. 23JHQ078). Supercomputing facilities were provided by Hefei Advanced Computing Center and Computing Center in Xi'an.

# REFERENCES

(1) Li, J.; Chen, M.; Cullen, D. A.; Hwang, S.; Wang, M.; Li, B.; Liu, K.; Karakalos, S.; Lucero, M.; Zhang, H.; Lei, C.; Xu, H.; Sterbinsky, G. E.; Feng, Z.; Su, D.; More, K. L.; Wang, G.; Wang, Z.; Wu, G. Atomically dispersed manganese catalysts for oxygen reduction in proton-exchange membrane fuel cells. Nat. Catal. 2018, 1 (12), 935-

(2) Wang, Z.; Niu, H.; Wu, T.; Ding, S.; Yu Xia, B.; Su, Y. Periodic Defect Boundary-Mediated Activity of Electrocatalytic Oxygen Reduction Reactions of Fe-N-C Catalysts. Renewables 2024, 2, 213.

(3) Liu, W.; Zhang, L.; Liu, X.; Liu, X.; Yang, X.; Miao, S.; Wang, W.; Wang, A.; Zhang, T. Discriminating Catalytically Active FeNx Species of Atomically Dispersed Fe-N-C Catalyst for Selective Oxidation of the C-H Bond. J. Am. Chem. Soc. 2017, 139 (31), 10790-10798.

(4) Zeng, Y.; Li, C.; Li, B.; Liang, J.; Zachman, M. J.; Cullen, D. A.; Hermann, R. P.; Alp, E. E.; Lavina, B.; Karakalos, S.; Lucero, M.; Zhang, B.; Wang, M.; Feng, Z.; Wang, G.; Xie, J.; Myers, D. J.; Dodelet, J.-P.; Wu, G. Tuning the thermal activation atmosphere breaks the activity-stability trade-off of Fe-N-C oxygen reduction fuel cell catalysts. Nat. Catal. 2023, 6 (12), 1215-1227.

(5) Yin, S.; Li, Y.; Yang, J.; Liu, J.; Yang, S.; Cheng, X.; Huang, H.; Huang, R.; Wang, C. T.; Jiang, Y.; Sun, S. Unveiling Low

- Temperature Assembly of Dense Fe-N4 Active Sites via Hydrogenation in Advanced Oxygen Reduction Catalysts. *Angew. Chem., Int. Ed.* **2024**, 63 (23), No. e202404766.
- (6) Liu, J.; Yang, J.; Dou, Y.; Liu, X.; Chen, S.; Wang, D. Deactivation Mechanism and Mitigation Strategies of Single-Atom Site Electrocatalysts. *Adv. Mater.* **2025**, *37* (27), 2420383.
- (7) Wu, G.; Zelenay, P. Activity versus stability of atomically dispersed transition-metal electrocatalysts. *Nat. Rev. Mater.* **2024**, 9 (9), 643–656.
- (8) Wan, X.; Shui, J. Exploring Durable Single-Atom Catalysts for Proton Exchange Membrane Fuel Cells. *ACS Energy Lett.* **2022**, 7 (5), 1696–1705.
- (9) Hu, X.; Chen, S.; Chen, L.; Tian, Y.; Yao, S.; Lu, Z.; Zhang, X.; Zhou, Z. What is the Real Origin of the Activity of Fe-N-C Electrocatalysts in the O2 Reduction Reaction? Critical Roles of Coordinating Pyrrolic N and Axially Adsorbing Species. *J. Am. Chem. Soc.* 2022, 144 (39), 18144–18152.
- (10) Di Liberto, G.; Giordano, L.; Pacchioni, G. Predicting the Stability of Single-Atom Catalysts in Electrochemical Reactions. *ACS Catal.* **2024**, *14* (1), 45–55.
- (11) Dobrota, A. S.; Skorodumova, N. V.; Mentus, S. V.; Pašti, I. A. Surface pourbaix plots of M@N4-graphene single-atom electrocatalysts from density functional theory thermodynamic modeling. *Electrochim. Acta* 2022, 412, 140155.
- (12) Yang, N.; Peng, L.; Li, L.; Li, J.; Liao, Q.; Shao, M.; Wei, Z. Theoretically probing the possible degradation mechanisms of an FeNC catalyst during the oxygen reduction reaction. *Chem. Sci.* **2021**, 12 (37), 12476–12484.
- (13) Chenitz, R.; Kramm, U. I.; Lefèvre, M.; Glibin, V.; Zhang, G.; Sun, S.; Dodelet, J.-P. A specific demetalation of Fe—N4catalytic sites in the micropores of NC\_Ar + NH3is at the origin of the initial activity loss of the highly active Fe/N/C catalyst used for the reduction of oxygen in PEM fuel cells. *Energy Environ. Sci.* **2018**, *11* (2), 365–382.
- (14) Kienitz, B.; Pivovar, B.; Zawodzinski, T.; Garzon, F. H. Cationic Contamination Effects on Polymer Electrolyte Membrane Fuel Cell Performance. *J. Electrochem. Soc.* **2011**, *158* (9), B1175.
- (15) Zhao, J.; Tu, Z.; Chan, S. H. Carbon corrosion mechanism and mitigation strategies in a proton exchange membrane fuel cell (PEMFC): A review. *J. Power Sources* **2021**, 488, 229434.
- (16) Zhuo, H.-Y.; Zhang, X.; Liang, J.-X.; Yu, Q.; Xiao, H.; Li, J. Theoretical Understandings of Graphene-based Metal Single-Atom Catalysts: Stability and Catalytic Performance. *Chem. Rev.* **2020**, *120* (21), 12315–12341.
- (17) Kumar, K.; Dubau, L.; Mermoux, M.; Li, J.; Zitolo, A.; Nelayah, J.; Jaouen, F.; Maillard, F. On the Influence of Oxygen on the Degradation of Fe-N-C Catalysts. *Angew. Chem., Int. Ed.* **2020**, *59* (8), 3235.
- (18) Choi, C. H.; Lim, H.-K.; Chung, M. W.; Chon, G.; Ranjbar Sahraie, N.; Altin, A.; Sougrati, M.-T.; Stievano, L.; Oh, H. S.; Park, E. S.; Luo, F.; Strasser, P.; Dražić, G.; Mayrhofer, K. J. J.; Kim, H.; Jaouen, F. The Achilles' heel of iron-based catalysts during oxygen reduction in an acidic medium. *Energy Environ. Sci.* **2018**, *11* (11), 3176–3182.
- (19) Zhang, G.; Chenitz, R.; Lefèvre, M.; Sun, S.; Dodelet, J.-P. Is iron involved in the lack of stability of Fe/N/C electrocatalysts used to reduce oxygen at the cathode of PEM fuel cells? *Nano Energy* **2016**, 29, 111–125.
- (20) Möller, S.; Barwe, S.; Masa, J.; Wintrich, D.; Seisel, S.; Baltruschat, H.; Schuhmann, W. Online Monitoring of Electrochemical Carbon Corrosion in Alkaline Electrolytes by Differential Electrochemical Mass Spectrometry. *Angew. Chem., Int. Ed.* **2020**, *59* (4), 1585–1589.
- (21) Ku, Y.-P.; Ehelebe, K.; Hutzler, A.; Bierling, M.; Böhm, T.; Zitolo, A.; Vorokhta, M.; Bibent, N.; Speck, F. D.; Seeberger, D.; Khalakhan, I.; Mayrhofer, K. J. J.; Thiele, S.; Jaouen, F.; Cherevko, S. Oxygen Reduction Reaction in Alkaline Media Causes Iron Leaching from Fe-N-C Electrocatalysts. J. Am. Chem. Soc. 2022, 144 (22), 9753–9763.

- (22) Kumar, K.; Dubau, L.; Jaouen, F.; Maillard, F. Review on the Degradation Mechanisms of Metal-N-C Catalysts for the Oxygen Reduction Reaction in Acid Electrolyte: Current Understanding and Mitigation Approaches. *Chem. Rev.* **2023**, *123* (15), 9265–9326.
- (23) Xu, H.; Wang, D.; Yang, P.; Liu, A.; Li, R.; Li, Y.; Xiao, L.; Ren, X.; Zhang, J.; An, M. Atomically dispersed M—N—C catalysts for the oxygen reduction reaction. *J. Mater. Chem. A* **2020**, 8 (44), 23187—23201.
- (24) Ramaswamy, N.; Mukerjee, S. Influence of Inner- and Outer-Sphere Electron Transfer Mechanisms during Electrocatalysis of Oxygen Reduction in Alkaline Media. *J. Phys. Chem. C* **2011**, *115* (36), 18015–18026.
- (25) Song, Y.; Yu, C.; Ma, D.; Liu, K. Recent progress on ZIF-8 based MOF derivatives for electrocatalysis. *Coord. Chem. Rev.* **2024**, 499, 215492.
- (26) Mehmood, A.; Gong, M.; Jaouen, F.; Roy, A.; Zitolo, A.; Khan, A.; Sougrati, M.-T.; Primbs, M.; Bonastre, A. M.; Fongalland, D.; Drazic, G.; Strasser, P.; Kucernak, A. High loading of single atomic iron sites in Fe–NC oxygen reduction catalysts for proton exchange membrane fuel cells. *Nat. Catal.* **2022**, *5* (4), 311–323.
- (27) Li, Y.; Chen, M.-Y.; Lu, B.-A.; Wu, H.-R.; Zhang, J.-N. Unravelling the role of hydrogen peroxide in pH-dependent ORR performance of Mn-N-C catalysts. *Appl. Catal., B* **2024**, 342, 123458.
- (28) Chinchilla, L.; Manzorro, R.; Olmos, C.; Chen, X.; Calvino, J. J.; Hungría, A. B. Temperature-driven evolution of ceria-zirconia-supported AuPd and AuRu bimetallic catalysts under different atmospheres: insights from IL-STEM studies. *Nanoscale* **2023**, *16* (1), 284–298.
- (29) Hrnjic, A.; Kamšek, A. R.; Pavlišič, A.; Šala, M.; Bele, M.; Moriau, L.; Gatalo, M.; Ruiz-Zepeda, F.; Jovanovič, P.; Hodnik, N. Observing, tracking and analysing electrochemically induced atomic-scale structural changes of an individual Pt-Co nanoparticle as a fuel cell electrocatalyst by combining modified floating electrode and identical location electron microscopy. *Electrochim. Acta* 2021, 388, 138513.
- (30) Malis, T.; Cheng, S. C.; Egerton, R. F. EELS log-ratio technique for specimen-thickness measurement in the TEM. *J. Electron Microsc. Tech.* **1988**, 8 (2), 193–200.
- (31) Sainio, S.; Wester, N.; Aarva, A.; Titus, C. J.; Nordlund, D.; Kauppinen, E. I.; Leppänen, E.; Palomäki, T.; Koehne, J. E.; Pitkänen, O.; Kordas, K.; Kim, M.; Lipsanen, H.; Mozetič, M.; Caro, M. A.; Meyyappan, M.; Koskinen, J.; Laurila, T. Trends in Carbon, Oxygen, and Nitrogen Core in the X-ray Absorption Spectroscopy of Carbon Nanomaterials: A Guide for the Perplexed. *J. Phys. Chem. C* **2021**, *125* (1), 973–988.
- (32) Rodil, S. E.; Muhl, S. Bonding in amorphous carbon nitride. *Diamond Relat. Mater.* **2004**, *13* (4–8), 1521–1531.
- (33) Ku, Y.-P.; Kumar, K.; Hutzler, A.; Götz, C.; Vorochta, M.; Sougrati, M. T.; Lloret, V.; Ehelebe, K.; Mayrhofer, K. J. J.; Thiele, S.; Khalakhan, I.; Böhm, T.; Jaouen, F.; Cherevko, S. Impact of Carbon Corrosion and Denitrogenation on the Deactivation of Fe–N–C Catalysts in Alkaline Media. *ACS Catal.* **2024**, *14* (11), 8576–8591.
- (34) Li, Y.; Li, J.; Wang, Y.-G.; Chen, X.; Liu, M.; Zheng, Z.; Peng, X. Carbon corrosion mechanism on nitrogen-doped carbon support A density functional theory study. *Int. J. Hydrogen Energy* **2021**, *46* (24), 13273–13282.
- (35) Qin, Y.; Zhao, W.; Xia, C.; Yu, L. J.; Song, F.; Zhang, J.; Wu, T.; Cao, R.; Ding, S.; Xia, B. Y.; Su, Y. CO Intermediate-Assisted Dynamic Cu Sintering During Electrocatalytic CO2 Reduction on Cu–N–C Catalysts. *Angew. Chem., Int. Ed.* **2024**, 63 (23), No. e202404763.
- (36) Manzorro, R.; Xu, Y.; Vincent, J. L.; Rivera, R.; Matteson, D. S.; Crozier, P. A. Exploring Blob Detection to Determine Atomic Column Positions and Intensities in Time-Resolved TEM Images with Ultra-Low Signal-to-Noise. *Microsc. Microanal.* **2022**, 28 (6), 1917–1930.
- (37) Lazaridis, T.; Stühmeier, B. M.; Gasteiger, H. A.; El-Sayed, H. A. Capabilities and limitations of rotating disk electrodes versus

- membrane electrode assemblies in the investigation of electrocatalysts. *Nat. Catal.* **2022**, *5* (5), 363–373.
- (38) Gallenkamp, C.; Kramm, U. I.; Proppe, J.; Krewald, V. Calibration of computational Mössbauer spectroscopy to unravel active sites in FeNC catalysts for the oxygen reduction reaction. *Int. J. Quantum Chem.* **2020**, *121* (3), No. e26394.
- (39) Ni, L.; Gallenkamp, C.; Wagner, S.; Bill, E.; Krewald, V.; Kramm, U. I. Identification of the Catalytically Dominant Iron Environment in Iron- and Nitrogen-Doped Carbon Catalysts for the Oxygen Reduction Reaction. *J. Am. Chem. Soc.* **2022**, *144* (37), 16827–16840.
- (40) Li, X.; Cao, C.-S.; Hung, S.-F.; Lu, Y.-R.; Cai, W.; Rykov, A. I.; Miao, S.; Xi, S.; Yang, H.; Hu, Z.; Wang, J.; Zhao, J.; Alp, E. E.; Xu, W.; Chan, T.-S.; Chen, H.; Xiong, Q.; Xiao, H.; Huang, Y.; Li, J.; Zhang, T.; Liu, B. Identification of the Electronic and Structural Dynamics of Catalytic Centers in Single-Fe-Atom Material. *Chem.* 2020, 6 (12), 3440–3454.
- (41) Li, J.; Sougrati, M. T.; Zitolo, A.; Ablett, J. M.; Oğuz, I. C.; Mineva, T.; Matanovic, I.; Atanassov, P.; Huang, Y.; Zenyuk, I.; Di Cicco, A.; Kumar, K.; Dubau, L.; Maillard, F.; Dražić, G.; Jaouen, F. Identification of durable and non-durable FeNx sites in Fe-N-C materials for proton exchange membrane fuel cells. *Nat. Catal.* **2021**, *4* (1), 10–19.
- (42) Liu, S.; Li, C.; Zachman, M. J.; Zeng, Y.; Yu, H.; Li, B.; Wang, M.; Braaten, J.; Liu, J.; Meyer, H. M.; Lucero, M.; Kropf, A. J.; Alp, E. E.; Gong, Q.; Shi, Q.; Feng, Z.; Xu, H.; Wang, G.; Myers, D. J.; Xie, J.; Cullen, D. A.; Litster, S.; Wu, G. Atomically dispersed iron sites with a nitrogen—carbon coating as highly active and durable oxygen reduction catalysts for fuel cells. *Nat. Energy* **2022**, *7* (7), 652—663.
- (43) Yu, D.; Deng, L. Gaussian Mixture Models. In *Automatic Speech Recognition*; Yu, D., Deng, L., Eds.; Springer: London, 2015; pp 13–21.
- (44) Wan, L.; Zhao, K.; Wang, Y.-C.; Wei, N.; Zhang, P.; Yuan, J.; Zhou, Z.; Sun, S.-G. Molecular Degradation of Iron Phthalocyanine during the Oxygen Reduction Reaction in Acidic Media. *ACS Catal.* **2022**, *12* (18), 11097–11107.
- (45) Bouleghlimat, E.; Davies, P. R.; Davies, R. J.; Howarth, R.; Kulhavy, J.; Morgan, D. J. The effect of acid treatment on the surface chemistry and topography of graphite. *Carbon* **2013**, *61*, 124–133.
- (46) Yadav, A.; Kumar, R.; Yadav, K.; Thomas, N.; Mishra, M.; Sahoo, B. Synthesis, characterization and insights into the supercapacitive and electrocatalytic (OER) bi-functional properties of nitrogen-doped reduced graphene oxide using Dicyandiamide precursor. *Solid State Sci.* **2024**, 147, 107377.
- (47) Wu, W.; Zhang, W.; Long, Y.; Qin, J.; Ma, J. MOF-derived Fe—N—C with interconnected mesoporous structure for halonitrobenzenes hydrogenation: Role of Dicyandiamide on the growth of active sites and pore structure. *Microporous Mesoporous Mater.* **2021**, 328, 111472
- (48) Fu, T.; Liu, R.; Lv, J.; Li, Z. Influence of acid treatment on N-doped multi-walled carbon nanotube supports for Fischer—Tropsch performance on cobalt catalyst. *Fuel Process. Technol.* **2014**, *122*, 49–57.
- (49) Zhu, C.; Shi, Q.; Xu, B. Z.; Fu, S.; Wan, G.; Yang, C.; Yao, S.; Song, J.; Zhou, H.; Du, D.; Beckman, S. P.; Su, D.; Lin, Y. Hierarchically Porous M–N–C (M=Co and Fe) Single-Atom Electrocatalysts with Robust MN $_{\rm x}$  Active Moieties Enable Enhanced ORR Performance. Adv. Energy Mater. 2018, 8 (29), 1801956.
- (50) Liu, T.; Wang, Y.; Li, Y. How pH Affects the Oxygen Reduction Reactivity of Fe-N-C Materials. ACS Catal. 2023, 13 (3), 1717–1725.
- (51) Guo, D.; Shibuya, R.; Akiba, C.; Saji, S.; Kondo, T.; Nakamura, J. Active sites of nitrogen-doped carbon materials for oxygen reduction reaction clarified using model catalysts. *Science* **2016**, *351* (6271), 361–365.
- (52) Xue, L.; Li, Y.; Liu, X.; Liu, Q.; Shang, J.; Duan, H.; Dai, L.; Shui, J. Zigzag carbon as efficient and stable oxygen reduction electrocatalyst for proton exchange membrane fuel cells. *Nat. Commun.* **2018**, *9* (1), 3819.

(53) Bates, J. S.; Johnson, M. R.; Khamespanah, F.; Root, T. W.; Stahl, S. S. Heterogeneous M-N-C Catalysts for Aerobic Oxidation Reactions: Lessons from Oxygen Reduction Electrocatalysts. *Chem. Rev.* 2023, 123 (9), 6233–6256.

